Article

Cross-linked multifunctional bilayer polymer buffer for enhanced efficiency and stability in perovskite solar cells

Yuheng Li[1,8], Lin Li[1,2,8], Haipeng Zeng[1], Chunxiang Lan[1], Shaomin Yang[1], Ziwei Zheng[3], Miaomiao Zeng[1], Yingying Shi[1], Kai Gao[2], Lianmeng Cui[4], Rui Guo[3], Jing Guo[3,5], Bin Hu ® [1,6] ✉, Yaoguang Rong ® [4], Haibing Xie ® [7] ✉ & Xiong Li ® [1,3] ✉

Addressing the stability challenges induced by the chemical interactions between metal electrodes and perovskite components is essential for high-performance perovskite solar cells (PSCs). Herein, we design a bilayer multifunctional polymer buffer composed of polyethyleneimine (PEI) and 2-((2-methyl-3-(2-((2-methylbutanoyl)oxy)ethoxy)−3-oxopropyl)thio)−3-(methyl-thio)succinic acid (PDMEA), inserting into the interface of metal electrode/transporting layer. This buffer mitigates metal atom diffusion by forming thioether-metal-carboxyl chelation rings between the metal layer and PDMEA. Additionally, it facilitates efficient electron transport and suppresses interfacial recombination through an in-situ cross-linking between the carboxyl groups of PDMEA and the amine groups of PEI based on Lewis acid-base reaction. Consequently, this design effectively reduces undesirable metal/ion interdiffusion during device fabrication and operation. The resulting PSCs with the PEI/PDMEA buffer achieve certified power conversion efficiencies (PCEs) of 26.46% (0.1 cm^2) and 24.70% (1.01 cm^2), demonstrating enhanced thermal and operational stability. We anticipate that this buffer design strategy, which forms bilayer polymer buffers via cross-linking of polymers with distinct functionalities, will inspire the rational design of robust buffers for highly efficient and stable PSCs and other electronic devices.

Halide perovskite solar cells (PSCs) have emerged as a highly promising next-generation photovoltaic technology, distinguished by their optoelectronic properties and cost-effective manufacturing processes[1–4]. Single-junction PSCs have achieved a certified power conversion efficiency (PCE) exceeding 26%, representing a significant milestone in the development of this technology[5]. However, to achieve widespread commercial viability, ensuring long-term stability under diverse environmental stressors remains critical[6,7]. Recent research has predominantly focused on optimizing perovskite materials and refining the interfaces between the perovskite layer and charge

[1]Michael Grätzel Center for Mesoscopic Solar Cells, Wuhan National Laboratory for Optoelectronics, Huazhong University of Science and Technology (HUST), Wuhan 430074, China. [2]Institute of New Materials and Advanced Manufacturing, Beijing Academy of Science and Technology (BJAST), Beijing 100089, China. [3]School of Physics and Optoelectronic Engineering, Hainan University, Haikou 570228, China. [4]State Key Laboratory of Advanced Technology for Materials Synthesis and Processing, Wuhan University of Technology, Wuhan 430070 Hubei, China. [5]Center for Advanced Studies in Precision Instruments, Hainan University, Haikou 570228, China. [6]Shenzhen Huazhong University of Science and Technology Research Institute, Shenzhen 518057, China. [7]Institute for Advanced Study, Shenzhen University, Shenzhen 518060, China. [8]These authors contributed equally: Yuheng Li, Lin Li. ✉e-mail: bin.hu@hust.edu.cn; xhbxal2021@szu.edu.cn; xiongli@hust.edu.cn

transporting layers (CTLs) to enhance operational stability[8–11]. Despite substantial progress, PSCs continue to face a formidable challenge: irreversible degradation caused by the chemical interaction between metal electrodes and perovskite components[12–14]. The intricate dynamics manifest on two fronts. Firstly, metal atoms cause surface damage to the perovskite active layer during electrode deposition processes such as thermal or E-beam evaporation due to their high-energy states at elevated temperatures[15]. These atoms can subsequently migrate within the PSCs under the influence of heat and/or light activation[16]. Secondly, volatile halide anions from the perovskite material concurrently diffuse towards commonly employed metal electrodes (Au, Ag, and Cu), leading to metal corrosion and inducing a halide deficiency in the perovskite layer[17–21]. This diffusion may result in the formation of insulating metal halide species or defect states at the perovskite interface or within the bulk[22,23]. To address these challenges, introducing a buffer layer between the metal electrode and charge transport layers (CTLs) is an effective strategy. An ideal buffer should satisfy the following criteria: (1) intrinsic stability under realistic operational conditions of PSCs, including high temperatures, prolonged light exposure, and humidity; (2) a dense film free of pinholes; (3) strong adhesion with both the metal electrode and neighboring layers; (4) ohmic contact and efficient charge transport through the electrode/CTL interface; (5) mitigation of charge recombination at the electrode/CTL interface. In p-i-n inverted PSCs, bathocuproine (BCP) and SnO_x are widely used buffers for achieving high-efficiency devices. Nevertheless, BCP is a small molecule that exhibits instability at high temperatures, allowing metal atoms and ions to readily penetrate it, leading to the degradation of PSCs[24,25]. SnO_x buffer layers are thermally stable; however, their deposition via atomic layer deposition (ALD) is time-consuming and not cost-effective, making them unsuitable for large-scale fabrication. To date, various diffusion barriers have been developed, including carbon quantum dots[16], bismuth interlayers[22], ytterbium oxide[25], and organic corrosion inhibitors such as benzotriazole[26]. While these barriers effectively prevent the undesired diffusion of ions or metals during operation, they do not adequately balance charge transport and interfacial recombination in PSCs. Consequently, the search for a universally applicable chemical strategy to enhance stability by mitigating surface damage during device fabrication and preventing metal/ion interdiffusion during device operation, while maintaining high efficiency, remains an ongoing challenge critical to the commercialization of PSCs.

In this study, we introduce a bilayer polymer consisting of polyethyleneimine (PEI) and 2-((2-methyl-3-(2-((2-methylbutanoyl)oxy) ethoxy)-3-oxopropyl)thio)-3-(methylthio)succinic acid (PDMEA), which is inserted between the electron transport layer (ETL) and the electrode. The synthesis of PDMEA involves thiol-ene polymerization, utilizing dimercaptosuccinic acid (DMSA), which contains thioether and carboxyl groups, as the thiol component[27–29], and ethylene dimethacrylate (EGDMA), an economically viable ene agent, to complete the polymerization process (Fig. 1a, and Supplementary Fig. 1)[30]. The thioether and carboxyl groups in PDMEA coordinate with metals, forming chelated rings that effectively inhibit metal diffusion. The abundance of carboxyl groups in PDMEA facilitates cross-linking with the amine groups on the PEI interfacial layer through Lewis acid-base interactions, enhancing charge transport efficiency and reducing charge recombination at the interface. The in-situ cross-linking reaction between PDMEA and PEI results in a network polymer that acts as a robust buffer, protecting the perovskite layer from undesirable ion
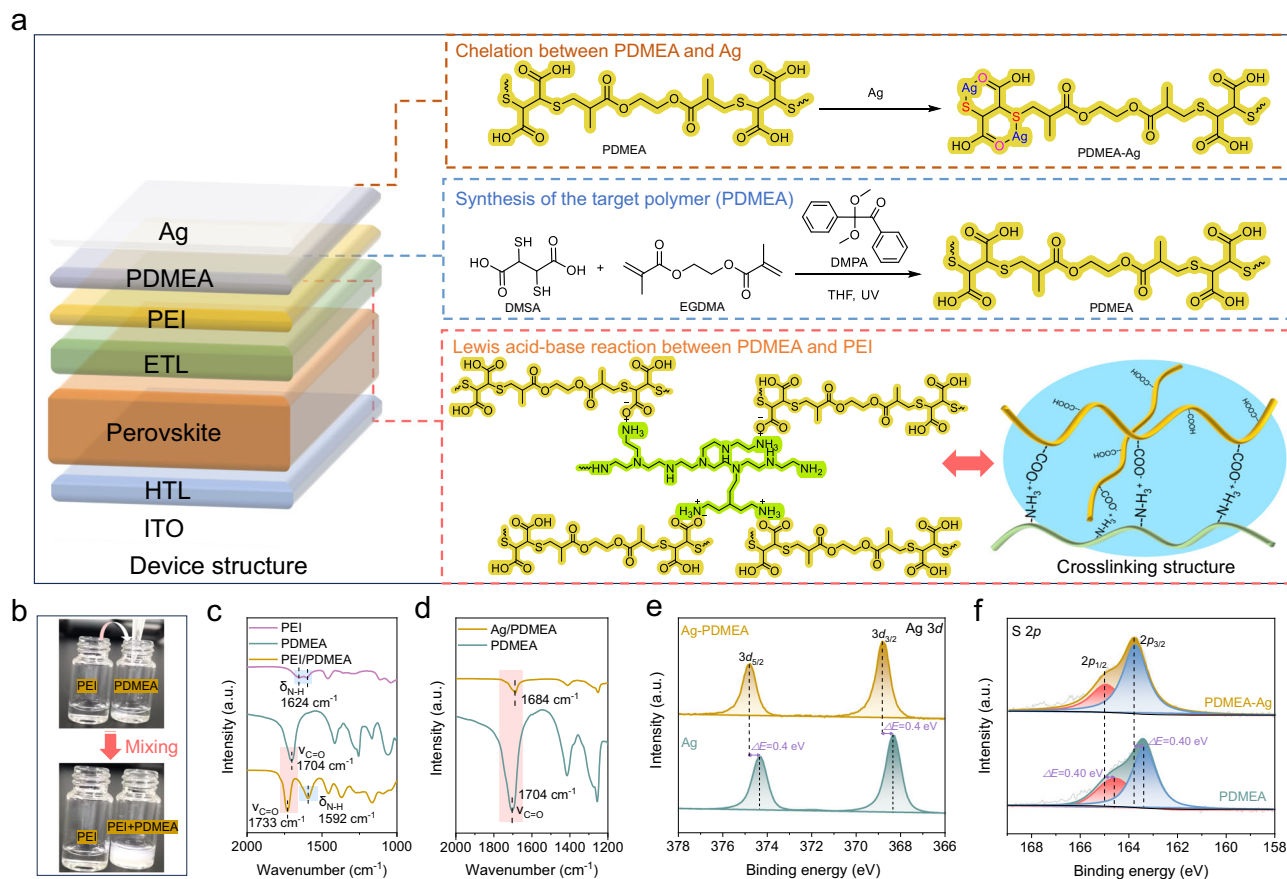
Fig. 1 | Molecular structure of PDMEA and interaction mechanism of PDMEA with PEI and Ag layers. a Schematic illustration of p-i-n PSC and molecular mechanism. **b** Photographs of PEI, PDMEA and PEI + PDMEA solutions respectively. **c** FTIR spectra of the PEI, PDMEA and PEI + PDMEA solutions respectively. **d** FTIR spectra of the PDMEA and Ag/PDMEA films respectively. **e, f** Ag 3d (**e**) and S 2p (**f**) XPS spectra of the Ag and Ag/PDMEA films.

diffusion. This collaborative effort leads to a significant improvement in device stability under both thermal and continuous illumination conditions. The devices incorporating PEI/PDMEA-based buffer layers exhibit PCEs of 26.54% (certified at 26.46%) and 24.86% (certified at 24.70%) for aperture areas of 0.1 cm² and 1.01 cm², respectively. PSCs equipped with PEI/PDMEA buffers retain over 90% of their initial efficiency after 2000 h at 85 °C and maintain 95.5% of their original efficiency after maximum power point tracking (MPPT) for 1010 h under 1 sun illumination at 65 °C. Furthermore, the versatility of the PEI/PDMEA buffer has been demonstrated in high-efficiency PSCs with various bandgaps, achieving champion PCEs of 19.26%, 26.54%, and 22.08% for absorbers with bandgaps of 1.75 eV, 1.53 eV, and 1.25 eV, respectively.

Results

Chemical design of bilayer polymer buffer PEI/PDMEA

We commence our design by initially selecting the PDMEA polymer to inhibit metal electrode diffusion, owing to its ability to capture heavy metals[27,28]. Subsequently, we test the performance of PSCs based on the PDMEA buffer and compare it to the efficiency of devices based on the prevalently utilized BCP buffer. Here, we employ a $Cs_{0.05}FA_{0.95}PbI_3$ perovskite as the light-absorbing material and construct PSCs in a p-i-n inverted configuration: glass/ITO/SAMs/perovskite/PCBM/buffer/Ag. The transparent conducting electrode utilizes tin-doped indium oxide (ITO), while the self-assembled monolayer (SAM) is 4-(7H-dibenzo[c,g]carbazol-7-yl)butyl)phosphonic acid (4PADCB). The [6,6]-phenyl-C_{61}-butyric acid methyl ester (PCBM) serves as the electron transporting layer (ETL). BCP or PDMEA is used as a buffer between the ETL and the electrode. The results indicate that compared with the devices based on the BCP buffer, the devices with the PDMEA buffer exhibit a 40 mV loss in open circuit voltage (V_{OC}) (averagely from 1.161 V to 1.123 V), suggesting an increased interfacial recombination at the ETL/metal electrode interface (Supplementary Fig. 2 and Supplementary Table 1). Similar short circuit current (Jsc) is observed, indicating benign carrier transport through the interface for both buffers. Hence, it is necessary to search for an interfacial material to address the severe interfacial recombination caused by the PDMEA buffer. Previously, PEI was utilized as an effective interfacial layer at the ETL/electrode interface to enhance the efficiency and stability of PSCs[31–33]. We hypothesize that the abundant amine groups of PEI are prone to cross-link with the carboxyl groups of PDMEA via Lewis acid-base reaction, forming a network polymer that serves as a robust buffer. Supplementary Fig. 2, 3 and Supplementary Table 1, 2 respectively present the device performance based on BCP, PEI, PDMEA and bilayer PEI/PDMEA buffer. Compared with BCP, PEI, and PDMEA buffer alone, the bilayer PEI/PDMEA buffer attains significantly enhanced V_{OC} and a slightly increased J_{SC} and FF. The results suggest that the bilayer PEI/PDMEA buffers alleviate the interfacial recombination problems of PEI and PDMEA when used independently and facilitate better charge transport through the interface. Given the efficiency achieved by the bilayer PEI/PDMEA buffer, in the subsequent sections, we will concentrate on comparing BCP and PEI/PDMEA buffer in terms of device efficiency and stability, as well as interfacial transport and recombination, with the aim of exploring the underlying mechanism of the bilayer buffer.

The detailed PDMEA synthesis process is described in Supplementary Fig. 1, with the reaction pathway and NMR results shown in Fig. 1a and Supplementary Fig. 4. The smooth charge transfer through the ETL/Ag interface is achieved by in-situ Lewis acid-base reactions between PDMEA and PEI, forming a cross-linked polymer (Fig. 1a). The validation of this reaction involves the analysis of a liquid reactant mixture containing PDMEA and PEI using Fourier Transform Infrared Spectroscopy (FTIR), characterizing the resulting solid adduct PDMEA-PEI (Fig. 1b, c, Supplementary Fig. 5). The FTIR spectra unveil noteworthy changes in the reactant structure. A higher

wavenumber at 1734 cm⁻¹ for the PDMEA-PEI adduct than the bare PDMEA at 1704 cm⁻¹ which contributed to vibration band of the carboxyl group ($v_{C=O}$) is observed. The blue-shift of the C = O frequency is a result of the reaction between PDMEA and PEI through carboxylic group and amine groups. Additionally, the pristine PEI spectrum exhibits a characteristic absorption at 1624 cm⁻¹, attributed to N-H bending vibrations in primary amine (-NH₂) groups, accompanied by a minor feature at 1592 cm⁻¹ that will be subsequently analyzed. Upon PDMEA incorporation, complete suppression of the 1624 cm⁻¹ signal occurs concurrently with significant intensification of the 1592 cm⁻¹ band. This spectral evolution aligns with the proposed Lewis acid-base interaction mechanism (Fig. 1a), where nucleophilic amine (-NH₂) groups from PEI react with carboxyl (-COOH) groups in PDMEA to generate ammonium (-NH₃⁺) and carboxylate (-COO⁻) species. The observed feature at 1592 cm⁻¹ falls within the characteristic 1600–1575 cm⁻¹ range for N−H bending vibrations in ammonium groups, confirming successful protonation of the amine groups. The weak 1592 cm⁻¹ signal in pure PEI samples likely originates from ambient moisture-induced partial protonation during atmospheric measurement, consistent with PEI's known hygroscopic nature. Collectively, the FTIR spectral (Fig. 1c) provide direct evidence of -NH₂ to -NH₃⁺ conversion, demonstrating effective in situ Lewis acid-base coordination between PEI and PDMEA components. This in-situ reaction not only strengthens the bottom-up contact through chemical interaction but also functions as a barrier that effectively suppresses the physical diffusion of metal.

The bi-functional groups in PDMEA, including thioether and carboxyl groups, enable chemical coordination with the silver electrode. FTIR spectra were utilized to discern the chemical states of the active adsorbing sites on PDMEA before and after coordination with silver. Figure 1d shows a red shift (1704 cm⁻¹ to 1684 cm⁻¹) in the absorption peak assigned to the stretching vibration of -C=O bonds in the COO⁻ groups of the pure PDMEA, indicating strong interactions between metal ions and the carboxyl groups on PDMEA. From the Ag $3d$ XPS spectra in Fig. 1e, we observed that the Ag $3d_{3/2}$ and Ag $3d_{5/2}$ peaks in the bare Ag film appear at 368.4 and 374.4 eV, respectively, while in the Ag-PDMEA film, the Ag $3d_{3/2}$ (368.8 eV) and Ag $3d_{5/2}$ (374.8 eV) peaks shift toward higher binding energy, indicating the chemical coordination between PDEMA and Ag. To comprehensively understand the chemical state of thioether groups bonded, Fig. 1f illustrates the XPS spectra of S $2p$ regions before and after coordination with Ag. In the PDMEA before coordination, peaks at a binding energy of 163.4 eV (S $2p_{3/2}$) and 164.6 eV (S$2p_{1/2}$) are attributed to C-S-C bonds. After post-coordination with Ag, these peaks partly shift to 163.8 eV (S $2p_{3/2}$) and 165.0 eV (S$2p_{1/2}$), respectively. Such an apparent binding energy shift indicates a pronounced interaction between thioether groups and Ag. According to FTIR and XPS results, the evidence of the obvious interactions between thioether, carboxyl groups and Ag, indicates the formation of chelated rings as schematically shown in Fig. 1a, agreeing well with previous reports[34]. Further comparative analysis of binding energies of BCP and PDMEA molecules was conducted on PbI₂-terminated FAPbI₃ perovskite and metallic silver surfaces through density functional theory (DFT) calculations (Supplementary Fig. 6). Both compounds demonstrate binding affinities to the PbI₂-terminated FAPbI₃ surface, with computed binding energies of −0.88 eV for BCP and −1.55 eV for PDMEA (Supplementary Fig. 6a, b, e). This reveals that PDMEA exhibits approximately twice the Pb²⁺ binding strength compared to BCP. Notably divergent behavior is observed on silver surfaces, where PDMEA displays a significantly stronger interaction (−2.19 eV) with Ag atoms compared to the BCP-Ag system, which shows a positive binding energy of +0.21 eV (Supplementary Fig. 6c, d, e), indicative of thermodynamic instability. These computational findings corroborate previous FTIR and XPS analyses, confirming PDMEA's chelation capability with both Pb²⁺ cations and silver atoms relative to BCP.

The enhanced binding characteristics of PDMEA are attributed to its optimized molecular structure for multidentate coordination with metal centers.

Further discussion will follow on how the PEI/PDMEA buffer effectively prevents metal diffusion in devices, elucidating its dual functionality as a protective layer during evaporation and a barrier against metal/ion diffusion during aging, contributing to the heightened performance and long-term reliability of the integrated system.

Mitigation of thermal damage during evaporation and metal/ion interdiffusion during aging

Concerns arose with the use of physical vapor deposition (PVD) methods directly depositing metal electrodes onto the semi-device. This posed a hidden risk for subsequent metal electrode penetration and thermal damage of perovskite surface. The PVD processes generated high-energy metal atoms, capable of penetrating many tens of nanometers into the fullerene layer[16,35,36]. The high energy release leads to damage of the perovskite surface, including component escape and the introduction of defects that adversely affect device efficiency and stability (Fig. 2a)[15,37,38].

To investigate the effect of electrode thermal evaporation, we conducted XPS, UV-vis and PL measurements on the perovskite. Prior to experimental measurements, the Ag film was removed with tape, and the buffer layers were rinsed with isopropanol (IPA, for BCP removal) or ethyl alcohol (EA, for PEI/PDMEA removal), and the ETL was removed by chlorobenzene (CB), exposing the bare perovskite surface. The component escape or diffusion from the perovskite surface was evident in XPS measurements, where the intensity of N 1s and I 3d peaks decreased in the BCP based device after thermal evaporation (Fig. 2b). In contrast, devices with PEI/PDMEA buffer retain almost the same intensity of N 1s and I 3d peaks, indicating the effective role of the buffer in mitigating the component escape during electrode evaporation (Fig. 2c). Note that the intensity of N 1s and I 3d was calibrated by C 1s peak intensity to minimize the impact of instrument-dependent signal intensity or other test conditions (Supplementary Fig. 7). To further assess thermal damage, UV-vis and PL measurements were employed (Fig. 2d, e). Results show that the BCP based device has a slight decrease in the absorbance and an obvious loss of PL intensity, indicating an increase of surface defects and recombination. Additional proofs on surface damage of perovskite in BCP based devices during evaporation can be seen in Supplementary Figs. 8, 9 and 10, which show the Ag penetration into PCBM layer (Supplementary Fig. 8) and the high energy release causes the right shift of (100) peak in XRD spectra (Supplementary Fig. 9) and TRPL lifetime decrease (Supplementary Fig. 11). Such effects are likely due to crystal lattice shrinkage and surface defects increase originated from the surface component escape or diffusion confirmed by XPS (Fig. 2b), Grazing Incidence X-Ray Diffraction (GIXRD) (Supplementary Fig. 12), and AFM-IR measurements (Supplementary Fig. 10). Nevertheless, devices with PEI/PDMEA buffer after thermal evaporation exhibit nearly unchanged intensity in UV-vis curves and a minor difference in PL intensity as the devices before thermal evaporation, effectively curtailing surface damage of the perovskite layers, preventing the formation of defects and associated defect-induced gap-states[22]. It should be noted that, although high-vacuum conditions also lead to surface damage of the perovskite layer, the damage brought by the high-vacuum thermal evaporation process is much more severe (Supplementary Fig. 13).

Preserving the integrity of the electrode against corrosion in a halogen-rich environment is imperative for the operational longevity of PSCs. The heightened susceptibility to light or thermal stress expedites the breakdown of lead-halide bonds, leading to the release of mobile halides within the perovskite layer[39]. The diffusion of these mobile halides outward poses a threat to the devices, particularly the Ag electrode, ultimately resulting in irreversible decomposition of the device.

The strong chemical or coordinated bond between PDMEA-PEI and PDMEA-Ag serves as a protective layer that inhibits metal/ion interdiffusion, significantly enhancing the corrosion resistance of the Ag electrode and perovskite layer. Previous reports have shown that the outward diffusion of iodide species migrate or diffuse through perovskite films and ETLs, eventually react with the metal electrodes and corroding them (forming AI$_x$, A = metal) under thermal or illuminated stress[22]. In our experiments, we prepared devices with the following structure: ITO/SAMs/perovskite/PCBM/buffer/Ag (15 nm), where the buffer is BCP or PEI/PDMEA. The samples were aged at 85 °C in the glove box for 500 h. The aging effect is checked by peeling off the Ag film and removing the buffers from the devices by IPA (removal of BCP) or by EA rinse (removal of PEI/PDMEA). SEM on the Ag film bottom shows pinholes in BCP based samples and dense morphology for PEI/PDMEA based samples (Fig. 2g), and EDS mapping of the exposed PCBM surface indicates a large amount of Ag in BCP based devices while negligible amount of Ag is observed in PEI/PDMEA samples (Fig. 2h). It is worth noting that samples with PEI alone were also examined by SEM and EDS mapping (Supplementary Figs. 14, 15), which shows similar results as those of devices with BCP. These findings suggest that the PEI/PDMEA buffer, formed through in-situ crosslinking, is more effective than both BCP and PEI in mitigating Ag diffusion. Time-of-flight secondary ion mass spectrometry (ToF-SIMS) was performed to further track the metal/ion diffusion within the devices. From Fig. 2i, we can clearly observe that the Ag and I ions in the aged BCP based device have migrated through the entire device, while the diffusion of these ions is largely blocked by the PEI/PDMEA buffer in the aged PEI/PDMEA device (Fig. 2j). Further removal of PCBM layer exposed the perovskite surface. XPS spectra were conducted and Pb^0 peak with a higher intensity in the BCP based one than that in the aged PEI/PDMEA based device was detected. This implies reduced deep defects in the latter (Supplementary Fig. 16)[40]. The schematic diagrams of metal/ion interdiffusion during aging with BCP or PEI/PDMEA buffer are present in Fig. 2f [37,38]. The suppressed metal/ion migration, combined with reduced chemical reaction at the electrode surface and perovskite/ETL heterojunctions, contributes to the improved stability of PEI/PDMEA based PSCs.

Carrier transport and recombination of devices with buffers

As mentioned in the introduction, buffers are essential for ensuring benign carrier transport and mitigating carrier recombination at the interfaces, which is critical for maintaining high efficiency of PSCs. Figures 3a, b show that PEI/PDMEA buffer layer exhibits a higher conductivity and mobility than those of BCP film, indicating better carrier transport through ETL/Ag interface[41,42]. This enhanced carrier transport of PEI/PDMEA buffer is also confirmed by C-AFM measurements (Supplementary Fig. 17). Moreover, TPC decay curves demonstrate a shorter photocurrent decay time in PEI/PDMEA based device compared with BCP based device (Fig. 3c and Supplementary Table 3), agreeing well with the enhanced carrier transport in the device with PEI/PDMEA buffer. Dark IV curves show the decreased reverse saturation current of PEI/PDMEA based device compared with BCP based PSCs, suggesting reduced carrier recombination in the interface (Fig. 3d). Built-in voltage (V_{bi}) can be obtained from Mott-Schottky curves, which shows that V_{bi} of PEI/PDMEA based device is 1.135 V, larger than 1.102 V of BCP based one, implying PEI/PDMEA buffer is beneficial for charge separation and collection (Fig. 3e), which is consistent with the ultraviolet photoelectron spectroscopy (UPS) results (Supplementary Fig. 18). Finally, TPV results show a longer photovoltage decay time in PEI/PDMEA based device compared to the device with BCP, indicating reduced carrier recombination (Fig. 3f and Supplementary Table 4), consistent with the dark IV measurements. The enhanced carrier transport and reduced carrier recombination of PEI/PDMEA buffer contribute to the performance improvement of PSCs, as will be discussed in the following section.
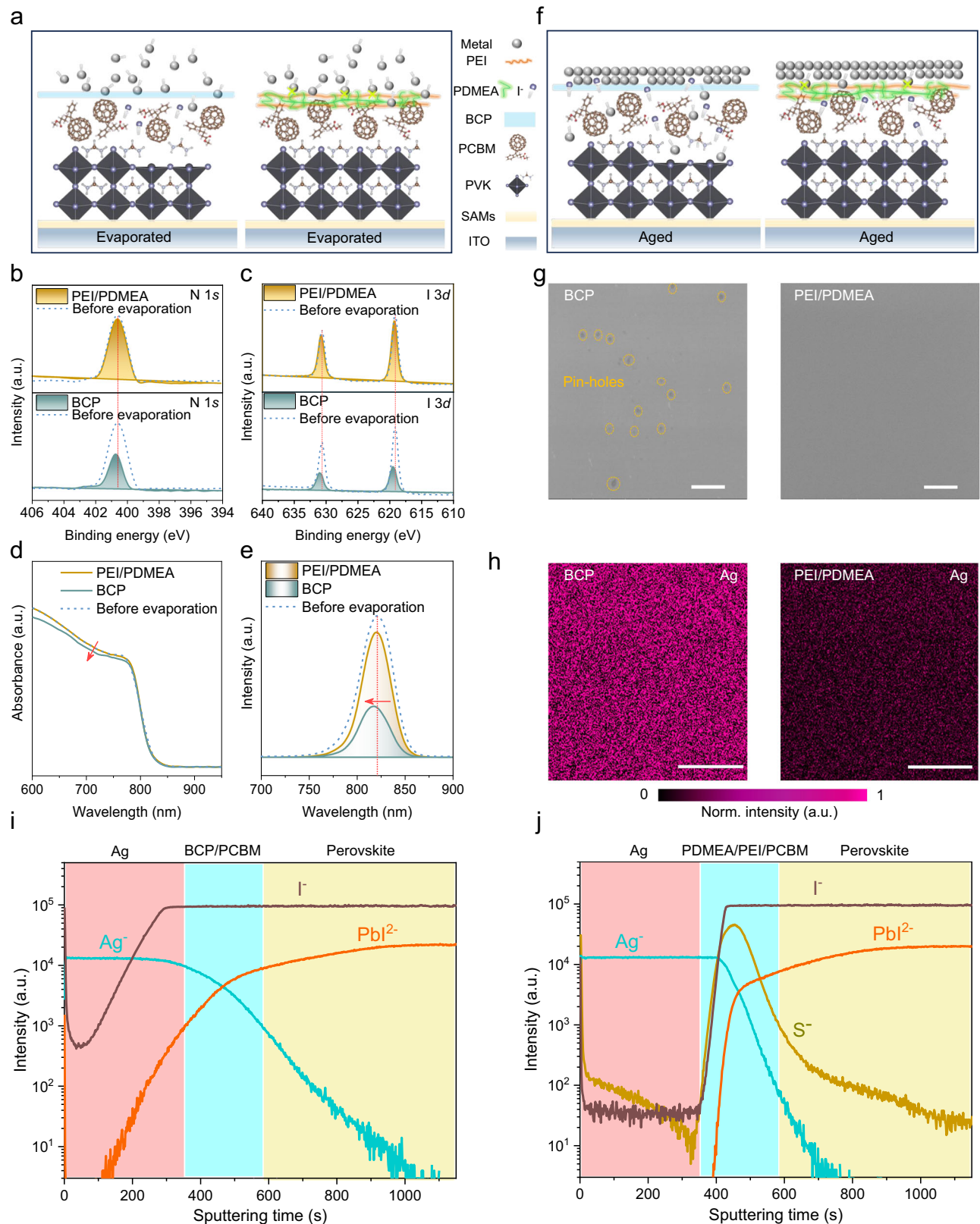
Fig. 2 | The stabilizing mechanism of PEI/PDMEA buffer. a Schematic illustration of PSCs during high-vacuum thermal evaporation of electrode, shows surface damage of perovskite film in BCP based device and intact perovskite layer in PEI/PDMEA based device. **b**, **c** XPS results of N 1s and I 3d peaks of perovskite layer before and after high-vacuum thermal evaporation of electrode. **d** UV-vis spectra of perovskite film before and after high-vacuum thermal evaporation of electrode. **e** PL spectra of perovskite film before and after high-vacuum thermal evaporation

of electrode. **f** Schematic illustration of complete solar cells after thermal aging, shows effective blocking of Ag and I diffusion in PEI/PDMEA based device.
g, **h** Peeled Ag experiments were performed on BCP and PEI/PDMEA based devices after aging at 85 °C for 500 h in glove box, (**g**) SEM images of the Ag film bottom and (**h**) EDS mapping of the PCBM film top. **i**, **j** The in-depth profile of ToF-SIMS for aged (**i**) BCP based and (**j**) PEI/PDMEA based device.
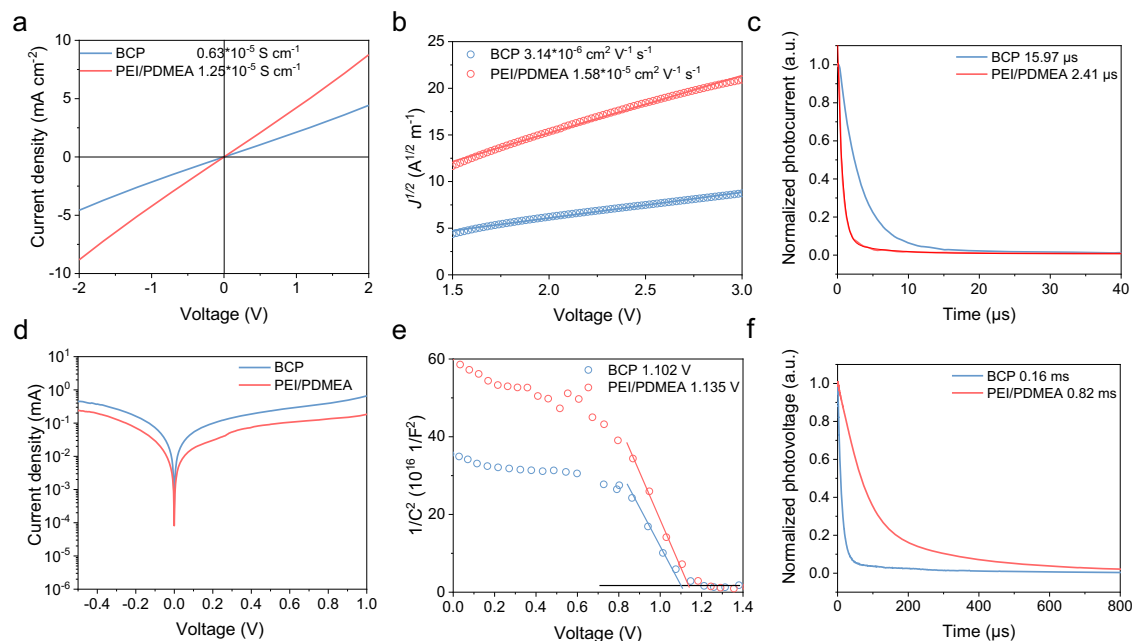
Fig. 3 | Electrical characterization of devices with buffers. a Conductivity measurement of BCP and PEI/PDMEA films. **b** Electron mobility for BCP and PEI/PDMEA films applying space charge-limited current (SCLC) method. The electron-only device structure is ITO/SnO$_2$/BCP or PEI/PDMEA/PCBM/Au. **c** Transient photocurrent (TPC) decay characteristics of the BCP and PEI/PDMEA based devices, respectively. **d** dark *J-V* curves of the BCP and PEI/PDMEA based PSCs, respectively. **e** Mott-Schottky curves of the BCP and PEI/PDMEA based PSCs, respectively. **f** Transient photovoltage (TPV) decay characteristics of the BCP and PEI/PDMEA based devices, respectively.

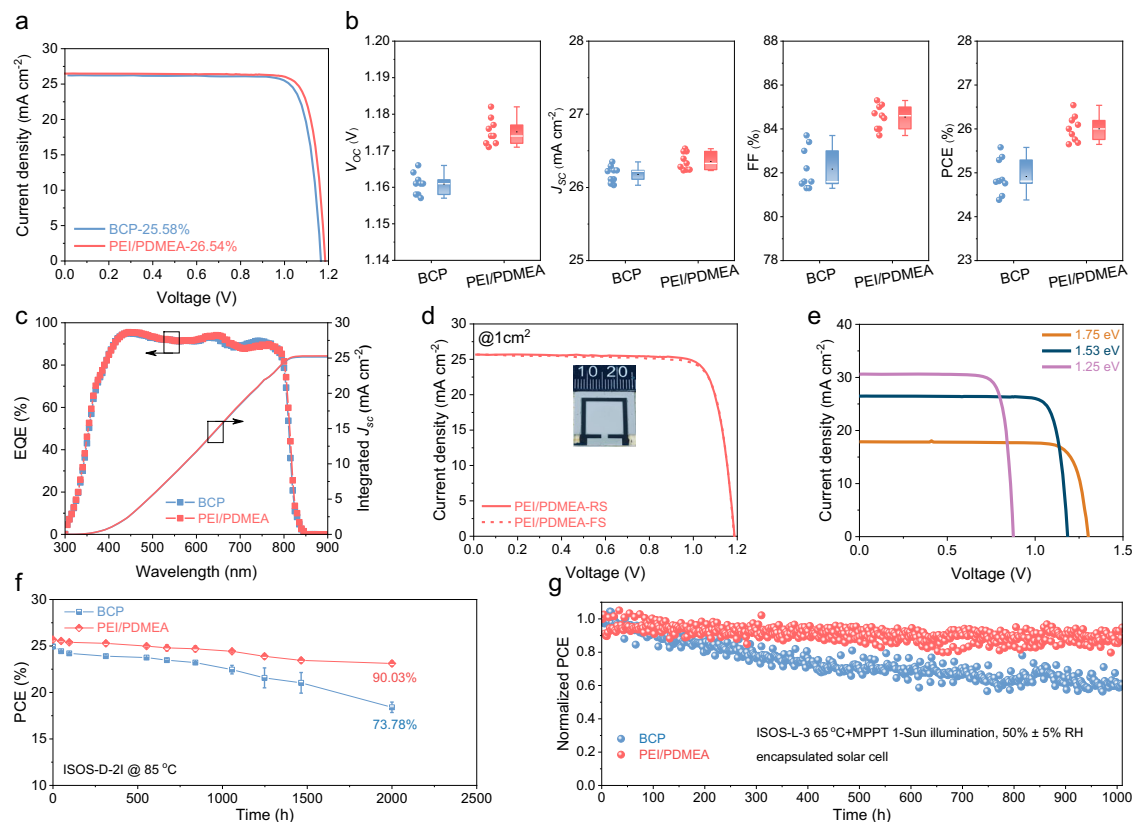## Performance and Stability of PSCs with buffers

Integral devices were assembled to investigate the influence of PEI/PDMEA buffer on device performance and stability. The device structures are ITO/HTL/perovskite/ETL/BCP/Ag and ITO/HTL/perovskite/ETL/PEI/PDMEA/Ag, respectively. Given that PDMEA is deposited by spin-coating, variations in PDMEA concentration (thickness) may impact device performance. Therefore, our initial investigation focuses on assessing the effect of PDMEA concentration on device performance. Supplementary Fig. 19 presents the photovoltaic parameter distribution of PSCs with different PDMEA concentrations (0.5, 1, 1.5 mg mL^{-1}). Detailed photovoltaic parameters can be found in Supplementary Table 5. It is observed that the best parameters in the PEI/PDMEA devices appear at the concentration of 0.5 mg mL^{-1}. However, with further increases in concentration, the fill factor (FF) decreases significantly, which correlates with a loss in J_{SC}. This is also consistent with the IV results of 1 cm^2 PSCs with various concentration of PDMEA (Supplementary Fig. 20 and Supplementary Table 6). We propose that at heavy concentration, the increased thickness of the insulating polymer hinders charge transport from the ETL to the electrode due to increased series resistance. We have further investigated the PEI concentration variations with PDMEA fixed to the optimized concentration of 0.5 mg mL^{-1}. Results show that the best concentration for the PEI/PDMEA bilayer buffer is 0.5 mg mL^{-1} for both PEI and PDMEA (Supplementary Fig. 21a). Additionally, the thickness of the PEI/PDMEA buffer is estimated to be around 4.5 nm by atomic force microscopy (AFM)(Supplementary Fig. 21b). Figure 4a, b presents the typical IV curves and statistical photovoltaic parameters of PSCs with BCP and PEI/PDMEA buffers, respectively. Detailed photovoltaic parameters can be seen in Supplementary Table 2 and Supplementary Figs. 2, 3. It clearly demonstrates that the PSCs with PEI/PDMEA buffer can achieve higher V_{OC} and FF and ultimately higher efficiency than the BCP based device, agreeing well with the reduced carrier recombination confirmed by dark IV and TPV results. Notably, a slight increase in average J_{SC} of PSCs with PEI/PDMEA buffer compared to device with BCP buffer can be seen from Fig. 4b and Supplementary Table 1, consistent with

the enhanced carrier transport proved previously. PSCs with PEI layers alone were also fabricated and IV measurements were performed, as is shown in Supplementary Figs. 2, 3. Results indicate that PSCs with PEI buffer have similar photovoltaic parameters with those of BCP based devices and are inferior to PEI/PDMEA based PSCs, confirming the enhanced performance of cross-linked PEI/PDMEA buffer.

Devices applying PEI/PDMEA buffer show a champion PCE up to 26.54 % (J_{SC} of 26.49 mA cm^{-2}, V_{OC} of 1.186 V, and FF of 84.49%) and a champion PCE of 24.86 % (J_{SC} of 25.74 mA cm^{-2}, V_{OC} of 1.182 V, and FF of 81.7%) for an aperture area of 0.1 cm^2 and 1.01 cm^2, respectively (Fig. 4a, Supplementary Fig. 20, Supplementary Table 2, 6), which are among the best performing PSCs in literature (Supplementary Fig. 22 and Supplementary Table 10). To the best of our knowledge, these efficiencies are the best for PSCs with various buffers, apart from those with traditional BCP and SnO$_x$ buffers (Supplementary Table 11). The J_{SC} of IV measurements (Fig. 4a) are consistent with the integrated J_{SC} extracted from incident photon-to-electron conversion efficiency (IPCE) spectra (Fig. 4c). The certification by an independently accredited testing center, gives PCEs of 26.46% and 24.7% for PEI/PDMEA based PSCs with an aperture area of 0.1 cm^2 and 1.01 cm^2, respectively (Fig. 4d, Supplementary Figs. 23, 24 and Supplementary Table 7). Our experiments further validate the universality of the PEI/PDMEA buffer in p-i-n PSCs with perovskite absorbers of various bandgaps, achieving champion PCEs of 19.26%, 26.54% and 22.08% for absorbers with bandgaps of 1.75 eV, 1.53 eV and 1.25 eV, respectively (Fig. 4e and Supplementary Fig. 25). Detailed parameters are present in Supplementary Table 8 and Supplementary Table 9, which are among the state-of-the art efficiencies for those bandgaps. In addition, the universal application of the PEI/PDMEA bilayer polymer buffer with different electrode materials, i.e., Au, Cu, and Ag is also performed (Supplementary Fig. 26), demonstrating that the devices based on PEI/PDMEA bilayer buffer achieve higher performance than those based on BCP buffer when using the same electrode.

To verify the feasibility of using PEI/PDMEA buffer in enhancing device stability, we conducted a comprehensive study on the PSCs

Fig. 4 | Photovoltaic performance and stability of PSCs with buffers. a J-V curves of the BCP and PEI/PDMEA-based device. **b** The PV parameters statistic of BCP and PEI/PDMEA devices. The boxes show the 25th and 75th percentiles, and the whiskers display the 5th and 95th percentiles. The median and mean are indicated by the dividing lines across the boxes and the open square symbols, respectively. The maximum and minimum values are represented by the cross symbols. **c** IPCE spectra of BCP and PEI/PDMEA PSCs. **d** J-V curve of the certified PEI/PDMEA-based device with an active area of 1.01 cm² and the inset shows a photograph of the device. **e** $J - V$ characteristics of the p-i-n PSCs with absorbers of various bandgaps applying PEI/PDMEA buffer. **f** Thermal stability during storage at 85 °C for 2000 h following ISOS-D-2I protocol. Four samples were applied for BCP and PEI/PDMEA groups, respectively, and the data is plotted with standard deviations (SD). **g** MPP tracking of encapsulated BCP and PEI/PDMEA devices under simulated 1-sun illumination at 50% relative humidity (RH) and 65 °C following ISOS-L-3 protocol.

under thermal and continuous illuminated stress conditions. We found that after 2000 h of thermal aging at 85 °C in nitrogen (following ISOS-D-2I protocol, where ISOS refers to the International Summit on Organic PV Stability), the PEI/PDMEA based devices retained 90% of the initial PCE, while the control device quickly reduced to 73.8% of its initial efficiency (Fig. 4f). To further evaluate operational stability, we conducted ISOS-L-3 testing. Encapsulated devices were subjected to MPPT under continuous 1-sun equivalent illumination using an ultraviolet-free white light-emitting diode (LED) light source, at 50 ± 5% relative humidity and a temperature of 60 ± 5 °C (Fig. 4g). PEI/PDMEA based PSCs maintained 95.5% of the initial value after aging for 1010 h, whereas the control device kept only 60% of its initial PCE.

Beyond its critical role in enhancing the efficiency and stability of PSCs, the PEI/PDMEA buffer also demonstrates a significant capacity to coordinate with heavy metals, such as lead, effectively inhibiting lead leakage from damaged PSCs. Experiments confirmed that most of the Pb^{2+} ions from degraded devices could effectively be trapped by the chelation between Pb and PDMEA polymer (Supplementary Fig. 27). While there is room for further optimization of the Pb^{2+} trapping process, our findings present a promising strategy to simultaneously enhance the long-term operational stability of PSCs and mitigate Pb^{2+} leakage into the environment, supporting clean energy applications. Additionally, we also tried to prepare the mixture PEI@PDMEA buffer by mixing PEI and PDMEA. Results show that the mixture buffer can increase the efficiency and stability of PSCs (Supplementary Fig. 28), but bilayer PEI/PDMEA buffer is more effective, most probably due to

the distinct function that PDMEA forms chelation with Ag and PEI acts as a suitable interfacial layer.

As outlined in the manuscript introduction, optimal bilayer buffers interposed between electrodes and charge transport layers must fulfill five critical requirements. Based on these criteria, we propose the following design principles for bilayer buffer systems in PSCs:

(1). Electrode/upper layer: the upper buffer layer must demonstrate strong interfacial coupling with metallic electrodes, preferably through covalent bond formation, to ensure low contact resistance and interfacial stability.

(2). ETL/lower layer: the lower buffer layer should serve as an effective defect-passivation interface between the upper buffer and ETL, simultaneously suppressing non-radiative recombination losses while maintaining energy level alignment.

(3). Upper layer/lower layer coupling: the lower layer must establish robust chemical/electronic interactions with the upper buffer layer to facilitate favorable charge carrier transport across the bilayer interface.

(4). Operational stability: the composite bilayer architecture requires thermal/photo-stability under device operational conditions.

These synergistic design principles emphasize the necessity of tailored chemical interactions, defect management, and thermal/photo-stability in developing high-performance buffer systems for next-generation PSCs. The hierarchical structure addresses both

interfacial recombination and carrier transport challenges inherent to perovskite photovoltaic devices.

Discussion

In summary, we have successfully developed a multifunctional PEI/PDMEA buffer layer for inverted PSCs. The thioether and carboxyl groups of PDMEA cooperatively coordinate with metal atom to form chelated rings, effectively immobilizing them. The cross-linking network of bilayer PEI/PDMEA buffer significantly inhibits the interdiffusion of metal/ions (Ag, I) and prevents the leakage of toxic heavy metals (Pb). PSCs incorporating the PEI/PDMEA buffer achieve certified PCEs of 26.46% and 24.7% for aperture areas of 0.1 cm^2 and 1.01 cm^2, respectively. These devices maintain over 90% of their initial efficiency after 2000 h at 85 °C and retain 95.5% of their original efficiency after MPPT for 1010 h under one-sun illumination at 65 °C. Furthermore, the PEI/PDMEA polymer is versatile and applicable to PSCs with various bandgaps, achieving champion PCEs of 19.26%, 26.54%, and 22.08% for 1.75 eV, 1.53 eV, and 1.25 eV perovskite absorbers, respectively. This demonstrates the universal applicability of the bilayer polymer buffer in enhancing the efficiency of PSCs. The buffer strategy, which involves in-situ cross-linking of polymers with distinct functionalities via Lewis acid-base reactions, may inspire the chemical design of robust buffers for interfacial stability and benign electronic properties in PSCs and other electronic devices.

Methods

Materials

Dimethyl formamide (DMF, 99.8%), dimethyl sulfoxide (DMSO, 99.8%), chlorobenzene (CB, 99.8%), and tetrahydrofuran (THF, 99.8%) were purchased from Acros. Lead iodide (PbI$_2$, 99.99%), cesium iodide (CsI, 99.99%), bathocuproine (BCP) and [2-(9H-Carbazol-9-yl) ethyl] [4-(7H-dibenzo[c,g]carbazol-7-yl)butyl)phosphonic acid (4PADCB) were purchased from TCI. Poly ethylenimine (PEI, Mw 25000) was purchased from Sigma-Aldrich. Formamidinium iodide (FAI) was purchased from Greatcell Solar Materials. PC$_{61}$BM was purchased from Xi'an Yuri Solar Co., Ltd. Indium tin oxide (ITO) (transmission>95%) substrates were purchased from Yingkou OPV Tech Co., Ltd. Dimercaptosuccinic acid (DMSA, 98%) was purchased from Energy Chemical Co., Ltd (China). 2, 2-dimethoxy-2-phenylacetophenone (DMPA, 99%) and ethylene dimethacrylate (EGDMA) were bought from Aladdin Chemical Co., Ltd. (China). Ag (99.999%) was purchased from ZhongNuo Advanced Material (Beijing) Technology Co. Ltd. All the materials were used as received unless specified.

Preparation of precursors

For the normal bandgap perovskite (E$_g$ = 1.53 eV): 1.5 M FA$_{0.95}$Cs$_{0.05}$PbI$_3$ normal-bandgap perovskite solution was prepared by dissolving 245.06 mg FAI, 19.50 mg CsI and 691.50 mg PbI$_2$ as additive in DMF/DMSO solvent (v/v = 4:1). The precursor solution was stirred at 60 °C for 1 h and then filtered by a 0.22 μm Polytetrafluoroethylene (PTFE) membrane before use.

For the wide bandgap perovskite (E$_g$ = 1.75 eV): 1.2 M FA$_{0.8}$Cs$_{0.2}$Pb(I$_{0.6}$Br$_{0.4}$)$_3$ wide-bandgap perovskite solution was prepared by dissolving 0.96 mmol FAI, 0.24 mmol CsI, 0.48 mmol PbI$_2$, 0.72 mmol PbBr$_2$ and 0.015 mmol Pb(SCN)$_2$ in 1 ml DMF: DMSO (3:1/v:v). The precursor solution was stirred at 60 °C for 1 h and then filtered by a 0.22 μm Polytetrafluoroethylene (PTFE) membrane before use.

For the narrow bandgap perovskite (E$_g$ = 1.25 eV): 1.8 M narrow-bandgap perovskite precursor solution was prepared by dissolving FA$_{0.6}$MA$_{0.3}$Cs$_{0.1}$Sn$_{0.5}$Pb$_{0.5}$I$_3$ was prepared by dissolving 0.18 mmol CsI, 1.08 mmol FAI, 0.54 mmol methylamine iodide, 0.90 mmol SnI$_2$, 0.90 mmol PbI$_2$, 0.09 mmol SnF$_2$, 0.036 mmol NH$_4$SCN and 0.036 mmol of glycine hydrochloride in mixed solvents of 750 μl DMF and 250 μl DMSO. The precursor solution was then stirred at 60 °C

overnight. The precursor solution was filtered by a 0.22 μm PTFE membrane before use.

Device fabrication

For the normal bandgap PSCs (E$_g$ = 1.53 eV): ITO glass (Universal Laser Systems, VLS2.30) were patterned by etching with a femtosecond laser. Then the glass substrates were cleaned by sequential ultra-sonication in a detergent solution, deionized water, and anhydrous ethanol. The substrates are dried using N$_2$ flow and treated with UV-Ozone for 30 min in air. SAMs (4PADCB, 0.5 mg mL^{-1} in ethyl alcohol) is spin-coated on ITO substrate at 3000 r.p.m for 30 s and then annealed at 100 °C for 10 min. After that, perovskite precursor solution was spin-coated on SAMs at 2000 rpm for 10 s and 4000 rpm for 40 s. The samples were immediately put on a preheated hot plate and annealed at 100 °C for 30 min in a nitrogen-filled glove box.

For the wide bandgap PSCs (E$_g$ = 1.75 eV): 4PADCB dissolved in ethanol (0.5 mg ml^{-1}) was filtered before the deposition and then 50 μl of the solution was dropped onto ITO substrate and spin-coated at 3000 rpm for 30 s, followed by annealing at 100 °C for 10 min. Then, 60 μl of the precursor was dropped on HTLs and quickly spin-coated through a two-step process—that is, 500 rpm for 2 s and 4000 rpm for 60 s and the antisolvent of 200 μl CB was dripped at 25 s of the second step. Then the as-prepared perovskite film was annealed at 100 °C for 10 min. For post-treatment passivation, 2-thiopheneethylammonium chloride dissolved in IPA (2 mg ml^{-1}) was spin-coated on the perovskite surface at 3000 rpm for 30 s after the as-prepared perovskite films were cooled down to room temperature, followed by annealing at 100 °C for 5 min.

For the narrow bandgap PSCs (E$_g$ = 1.25 eV): PEDOT:PSS films were coated on the cleaned ITO substrate at 4000 rpm for 50 s and then dried at 150 °C for 30 min. The NBG perovskite precursor was spin-coated on ITO/PEDOT:PSS at 1000 rpm for 10 s with an acceleration of 200 rpm s^{-1} in the first step and at 4000 rpm for 40 s with an acceleration of 1000 rpm s^{-1}. Then, 400 μl chlorobenzene was dripped onto the surface of the spinning substrate during the second spin coating step. All perovskite films were annealed at on a 100 °C hotplate for 10 min, followed by annealing at 65 °C for over 10 min. For post-treatment passivation, 1.0 mg of EDAI$_2$ was added to 1 mL of IPA and 1 mL of toluene. The mixed solvent solution was stirred at 70 °C for 3 h and then filtered through a 0.22 μm PTFE filter before spin coating. 120 μL of the EDAI$_2$ solution was applied to the annealed and cooled perovskite films by spin coating at 4000 rpm for 20 s with an acceleration of 1333 rpm s^{-1}. Following spin coating, the films were immediately annealed again at 100 °C for about 5 min.

In the subsequent technological steps, PSCs with three kinds of bandgaps follow the same processes. PC$_{61}$BM solution (20 mg in 1 mL CB) was spin-coated on top of the perovskite films at a speed of 2000 rpm for 40 s. Then we dynamically spin-coated BCP (0.5 mg·mL^{-1} in IPA) or PEI (0.5 mg·mL^{-1} in IPA) solution onto the surface of PC$_{61}$BM film at a speed of 5,000 rpm for 40 s. Afterwards the substrate was transferred to a vacuum chamber for Ag deposition (100 nm). For the PSCs with PDMEA, PDMEA solution (0,0.5,1,1.5 mg mL^{-1} in ethyl acetate) was spin coated onto PEI film surface at 5000 rpm for 30 s and then annealed at 75 °C for 10 min.

Measurement and Characterization

J-V measurements were conducted using a Keithley 2400 source meter. Simulated AM 1.5 G irradiation (100 mW cm^{-2}) was produced by a xenon-lamp-based solar simulator (Oriel 94023 A, Newport). The light intensity was calibrated by a standard silicon reference cell from Newport. A voltage scan was measured from 1.2 V to 0 V with a scanning rate of 0.05 V s^{-1}, and a voltage step of 10 mV was used. Thermal stability is recorded by storing the non-encapsulated devices on a hot

plate setting at 85 °C in the glovebox. The J-V curves are measured after cooling the PSCs down to room temperature. The operational stability test was carried out at the MPP for the encapsulated cells under AM 1.5 illumination (100 mW cm^{-2}). The cells were tested in a light soaking chamber, and the surface temperature of cells was controlled to be 60 ± 5 °C. The morphologies of PSCs were characterized using an SEM (Hitachi S-4300) at an accelerating voltage of 3-5 kV. The FTIR spectra were recorded with a VERTEX 70 Infrared Fourier transform microscope (Bruker Co., Germany). XPS spectra were measured by a Thermo-Fisher ESCALAB 250Xi system with a monochromatized Al Kα (for XPS mode) under a pressure of 5.0×10^{-7} Pa. The X-ray diffraction (XRD) patterns were collected from X-ray diffractometer (D8 Advance). Compositional depth profiling of perovskite solar cells was carried out using a ToF-SIMS 5 system from IONTOF, operated in the spectral mode and using a 30-keV Bi^{3+} primary ion beam with an ion current of 0.8 pA. For depth profiling, a 1-keV Cs$^+$ sputter beam with a current of 28 nA was used to remove material layer by layer in interlaced mode. The UV-vis spectra were measured by using a SolidSpec-3700 Ultraviolet-visible near-infrared spectrophotometer. Photoluminescence measurements (PL) were conducted using a mercury lamp (U-LH100HG, Olympus) as excitation after passing through a 460 to 490 nm band-pass filter. The excitation intensity under 100x objective was estimated to be 1.3 - 13.0 W cm^{-2}. The signals passed through a 520 nm long-pass filter before collected by a CCD camera (Tucsen, TCH-1.4CICE) and a spectrometer (Renishaw inVia). Time-resolved photoluminescence (TRPL) measurements employed a 70 ps pulsed laser (20 MHz) through the same 100× objective (NA = 0.90) and 520 nm long-pass filter as PL. Signals were time-resolved via single-photon counting system (<200 ps response), complementing mercury-lamp-excited PL (1.3 - 13.0 W cm^{-2}) on the integrated system. C-AFM was operated combined with a Cypher S AFM (Asylum Research, Oxford Instruments) and a HF2LI Lock-in amplifier (Zurich Instruments) in a N$_2$-filled glove box. The resonance frequency ω_0 and spring constant of AFM conducting tips are around 140 kHz and 5.0 N m^{-1}, respectively. Measurements of transient photocurrent (TPC) and transient photovoltage (TPV) were performed using a ZAHNER Zennium electrochemical analysis system coupled with an LED illumination module. ^{1}H NMR spectra were recorded on Bruker Avance III-400 MHz NMR spectrometer. Chemical shifts are reported in parts per million (ppm, δ).

First principles calculations
All calculations in this study were performed with the Vienna ab initio Simulation Package (VASP)[43] within the frame of density functional theory (DFT). The exchange-correlation interactions of electron were described via the generalized gradient approximation (GGA) with PBE functional[44], and the projector augmented wave (PAW) method[45] was used to describe the interactions of electron and ion. Additionally, the DFT-D3 method was used to account for the long-range van der Waals forces present within the system. The Monkhorst-Pack scheme[46] was used for the integration in the irreducible Brillouin zone. The kinetic energy cut-off of 450 eV was chosen for the plane wave expansion. The total energy was converged within 10^{-5} eV per formula unit and the final forces on all ions are less than 0.02/Å.

Pb^{2+} sorption kinetics of PDMEA
An activated sample of PDMEA (20 mg) and a freshly prepared aqueous solution of lead (II) nitrate (10.0 ppm, 50.0 mL) were mixed in a 100-mL round-bottom flask and stirred at room temperature. During the adsorption, the mixture was withdrawn and filtered at intervals through a 0.22 μm membrane filter for all samples (each sample of 0.5 mL), then each of the filtrates was diluted using DI water into 10 mL and quantified by ICP-OES to determine the remaining Pb^{2+} content. The amount of lead adsorbed per unit mass of PDMEA at time t, q_t was determined by

the equation:

$$q_t = V(C_0 - C_t)/m \qquad (1)$$

wherein C_0 and C_t (mmol L^{-1}) represent the initial concentration and after time t (min), respectively, m is the adsorbent mass (0.020 g) and V corresponds to the volume of the solution (0.005). The adsorption kinetics were analyzed by pseudo-second-order models. The curves drawn on top of the data are guides to the eye. The inset shows pseudo-second-order fitting results. The fitting is based on the pseudo-second-order equation:

$$t/q_t = 1/(kq_e)^2 + t/q_e \qquad (2)$$

wherein k is the pseudo-second order rate constant and q_e and q_t are the amounts of Pb^{2+} adsorbed at equilibrium and after time t, respectively.

Pb^{2+} sorption isotherm measurement of PDMEA
Lead (II) acetate solutions of various Pb^{2+} concentrations (10, 25, 50, 100, 250, 500, 750 and 1000 mg L^{-1}) were prepared using D.I. water, and used in the following adsorption procedure. An activated sample of PDMEA (5.0 mg) was added to each centrifuge tube containing Pb^{2+} solution (5.0 mL) with different concentrations. The mixtures were stirred at room temperature for 18 h. The polymer was separated by centrifugation and the supernatant was filtered through a 0.22 μm membrane and analyzed using ICP-OES to determine the remaining Pb^{2+} content. The saturated Pb adsorption capacity (q_{max}) is calculated by the following mathematical expression:

$$q_e = q_m K_L C_e/(1 + K_L C_e) \qquad (3)$$

where q_e (mg g^{-1}) is the sorption capacity at equilibrium state, C_e (mg L^{-1}) is the Pb concentration remaining in the solution at equilibrium state and K_L (L mg^{-1}) is a constant related to binding site affinity. Values for q_{max} (355 mg g^{-1}) and K_L can be obtained from the slope and y-intercept, respectively, by plotting C_e/q_e versus C_e.

Reporting summary
Further information on research design is available in the Nature Portfolio Reporting Summary linked to this article.

Data availability
The data that support the findings of this study are available in the Supplementary Information/Source Data file (Figshare: https://doi.org/10.6084/m9.figshare.28930643). All other data of this study are available from the corresponding authors upon request. Source data are provided with this paper.

References
1. Li, C. et al. Rational design of Lewis base molecules for stable and efficient inverted perovskite solar cells. *Science* **379**, 690–694 (2023).
2. Azmi, R. et al. Damp heat-stable perovskite solar cells with tailored-dimensionality 2D/3D heterojunctions. *Science* **376**, 73–77 (2022).
3. Green, M. et al. Solar cell efficiency tables (Version 63). *Prog. Photovolt.* **32**, 3–13 (2024).
4. Stranks, S. D. et al. Electron-hole diffusion lengths exceeding 1 micrometer in an organometal trihalide perovskite absorber. *Science* **342**, 341–344 (2013).
5. Green, M. et al. Solar cell efficiency tables (Version 65). *Prog. Photovolt.* **33**, 3–15 (2025).
6. Park, N.-G. et al. Towards stable and commercially available perovskite solar cells. *Nat. Energy* **1**, 135107 (2016).

7. Boyd, C. C. et al. Understanding degradation mechanisms and improving stability of perovskite *photovoltaics*. *Chem. Rev.* **119**, 3418–3451 (2019).

8. Zeng, H. et al. Improved performance and stability of perovskite solar modules by regulating interfacial ion diffusion with nonionic cross-linked 1D lead-iodide. *Adv. Energy Mater.* **12**, 2102820 (2022).

9. Luo, L. et al. Stabilization of 3D/2D perovskite heterostructures via inhibition of ion diffusion by cross-linked polymers for solar cells with improved performance. *Nat. Energy* **8**, 294–303 (2023).

10. Zheng, X. et al. Co-deposition of hole-selective contact and absorber for improving the processability of perovskite solar cells. *Nat. Energy* **8**, 462–472 (2023).

11. Jiang, Q. et al. Surface reaction for efficient and stable inverted perovskite solar cells. *Nature* **611**, 278–283 (2022).

12. Tress, W. et al. Interpretation and evolution of open-circuit voltage, recombination, ideality factor and subgap defect states during reversible light-soaking and irreversible degradation of perovskite solar cells. *Energy Environ. Sci.* **11**, 151–165 (2018).

13. Li, J. et al. Direct evidence of ion diffusion for the silver-electrode-induced thermal degradation of inverted perovskite solar cells. *Adv. Energy Mater.* **7**, 1602922 (2017).

14. Guo, H. et al. Immobilizing surface halide in perovskite solar cells via calix[4]pyrrole. *Adv. Mater.* **35**, 2301871 (2023).

15. Luo, C. et al. Eliminating performance loss from perovskite films to solar cells. *Sci. Adv.* **10**, eadp0790 (2024).

16. Bi, E. et al. Diffusion engineering of ions and charge carriers for stable efficient perovskite solar cells. *Nat. Commun.* **8**, 15330 (2017).

17. Kato, Y. et al. Silver iodide formation in methyl ammonium lead iodide perovskite solar cells with silver top electrodes. *Adv. Mater. Interfaces* **2**, 1500195 (2015).

18. Zhao, J. et al. Is Cu a stable electrode material in hybrid perovskite solar cells for a 30-year lifetime?. *Energy Environ. Sci.* **9**, 3650–3656 (2016).

19. Domanski, K. et al. Migration of cations induces reversible performance losses over day/night cycling in perovskite solar cells. *Energy Environ. Sci.* **10**, 604–613 (2017).

20. Besleaga, C. et al. Iodine migration and degradation of perovskite solar cells enhanced by metallic electrodes. *J. Phys. Chem. Lett.* **7**, 5168–5175 (2016).

21. Guerrero, A. et al. Interfacial degradation of planar lead halide perovskite solar cells. *ACS Nano* **10**, 218–224 (2016).

22. Wu, S. et al. A chemically inert bismuth interlayer enhances long-term stability of inverted perovskite solar cells. *Nat. Commun.* **10**, 1161 (2019).

23. Wang, Y. et al. Probing photoelectrical transport in lead halide perovskites with van der Waals contacts. *Nat. Nanotechnol.* **15**, 768–775 (2020).

24. Bai, S. et al. Planar perovskite solar cells with long-term stability using ionic liquid additives. *Nature* **571**, 245–250 (2019).

25. Chen, P. et al. Multifunctional ytterbium oxide buffer for perovskite solar cells. *Nature* **625**, 516–522 (2024).

26. Li, X. et al. Chemical anti-corrosion strategy for stable inverted perovskite solar cells. *Sci. Adv.* **6**, eabd1580 (2020).

27. Bai, L. et al. Remarkable colorimetric sensing of heavy metal ions based on thiol-rich nanoframes. *Chem. Commun.* **52**, 13691–13694 (2016).

28. Uygun, D. A. et al. Self-propelled chelation platforms for efficient removal of toxic metals. *Environ. Sci. Nano* **3** (2016).

29. Yantasee, W. et al. Direct detection of Pb in urine and Cd, Pb, Cu, and Ag in natural waters using electrochemical sensors immobilized with DMSA functionalized magnetic nanoparticles. *Analyst* **133**, 348–355 (2008).

30. Quinn, C. P. et al. Photo-crosslinked copolymers of 2-hydroxyethyl methacrylate, poly(ethylene glycol) tetra-acrylate and ethylene dimethacrylate for improving biocompatibility of biosensors. *Biomaterials* **16**, 389–396 (1995).

31. Dong, S. et al. Polyethylenimine as a dual functional additive for electron transporting layer in efficient solution processed planar heterojunction perovskite solar cells. *RSC Adv.* **6**, 57793–57798 (2016).

32. Zhou, Y. et al. Efficiently improving the stability of inverted perovskite solar cells by employing polyethylenimine-modified carbon nanotubes as electrodes. *ACS Appl. Mater. Interfaces* **10**, 31384–31393 (2018).

33. Dong, Y. et al. Interface reactive sputtering of transparent electrode for high-performance monolithic and stacked perovskite tandem solar cells. *Adv. Mater.* **36**, 2312704 (2024).

34. Huang, Y. et al. Thiol-ene synthesis of thioether/carboxyl-functionalized polymers for selective adsorption of silver (I) ions. *Chem. Eng. J.* **375**, 121935 (2019).

35. Sang, L. et al. Penetration and reaction depths of vapor deposited Ag, Mg, Al, and Ca on oligothiophene thin films. *Chem. Mater.* **31**, 6908–6917 (2019).

36. Zhang, G. et al. Extensive penetration of evaporated electrode metals into fullerene films: intercalated metal nanostructures and influence on device architecture. *ACS Appl. Mater. Interfaces* **7**, 25247–25258 (2015).

37. Anubhav, J. et al. The materials project: a materials genome approach to accelerating materials innovation. *APL Mater.* **1**, 011002 (2013).

38. Momma, K. et al. VESTA 3 for three-dimensional visualization of crystal, volumetric and morphology data. *J. Appl. Crystallogr.* **44**, 1272–1276 (2011).

39. Wei, Z. et al. Strategies for enhancing the stability of metal halide perovskite towards robust solar cells. *Sci. China Mater.* **65**, 3190–3201 (2022).

40. Bi, D. et al. Polymer-templated nucleation and crystal growth of perovskite films for solar cells with efficiency greater than 21. *Nat. Energy* **1**, 16142 (2016).

41. Yang, D. et al. Surface optimization to eliminate hysteresis for record efficiency planar perovskite solar cells. *Energy Environ. Sci.* **9**, 3071–3078 (2016).

42. Yang, D. et al. High efficiency planar-type perovskite solar cells with negligible hysteresis using EDTA-complexed SnO_2. *Nat. Commun.* **9**, 3239 (2018).

43. Kresse, G. et al. Efficient iterative schemes for Ab initio total-energy calculations using a plane-wave basis set. *Phys. Rev. B.* **54**, 11169–11186 (1996).

44. Perdew, J. P. et al. Generalized gradient approximation made simple. *Phys. Rev. Lett.* **77**, 3865–3868 (1996).

45. Kresse, G. et al. From ultrasoft pseudopotentials to the projector augmented-wave method. *Phys. Rev. B.* **59**, 1758–1775 (1999).

46. Monkhorst, H. J. et al. Special points for brillouin-zone integrations. *Phys. Rev. B.* **13**, 5188–5192 (1976).

Acknowledgements

Author contributions

X.L. and H.X. supervised the project and conceived the idea. Y.L. and L.L. designed the experiments and participated in discussing the results. Y.L. and L.L. fabricated the perovskite devices and characterized the devices. H. Z. synthesized polymer materials. L.C. and Y.R. contributed to the XPS test. C.L., M.Z. and Y.S. contributed to the TRPL mapping test and analysis. B.H., S.Y., Z.Z., J.G., R.G. and K.G. actively contributed to data analysis and discussions. Y.L., L.L., H.X. and X.L. contributed to the preparation of the manuscript. All authors discussed the results and commented on the manuscript.

Competing interests

The authors declare no competing interests.

Additional information

Supplementary information The online version contains supplementary material available at https://doi.org/10.1038/s41467-025-61294-z.

Correspondence and requests for materials should be addressed to Bin Hu, Haibing Xie or Xiong Li.

Peer review information *Nature Communications* thanks Zhan'ao Tan, and the other, anonymous, reviewer(s) for their contribution to the peer review of this work. A peer review file is available.

Reprints and permissions information is available at http://www.nature.com/reprints

Publisher's note Springer Nature remains neutral with regard to jurisdictional claims in published maps and institutional affiliations.